


Cite this: *Nanoscale*, 2023, **15**, 14409

Hybrid multifunctionalized mesostructured stellate silica nanoparticles loaded with β -diketonate $\text{Tb}^{3+}/\text{Eu}^{3+}$ complexes as efficient ratiometric emissive thermometers working in water†

Tristan Pelluau,^a Saad Sene,^a Lamiaa M. A. Ali,^{b,c} Gautier Félix,^a Faustine Manhes,^b Albano N. Carneiro Neto,^d Luis D. Carlos,^d Belén Albela,^e Laurent Bonneviot,^e Erwan Olivier,^a Magali Gary-Bobo,^b Yannick Guari^{*,a} and Joulia Larionova^{*,a}

Despite the great effort made in recent years on lanthanide-based ratiometric luminescent nanothermometers able to provide temperature measurements in water, their design remains challenging. We report on the synthesis and properties of efficient ratiometric nanothermometers that are based on mesoporous stellate nanoparticles (MSN) of *ca.* 90 nm functionalized with an acetylacetonate (acac) derivative inside the pores and loaded with β -diketonate- $\text{Tb}^{3+}/\text{Eu}^{3+}$ complexes able to work in water, in PBS or in cells. Encapsulating a $[(\text{Tb}/\text{Eu})_9(\text{acac})_{16}(\mu_3\text{-OH})_8(\mu_4\text{-O})(\mu_4\text{-OH})]$ complex (Tb/Eu ratio = 19/1 and 9/1) led to hybrid multifunctionalized nanoparticles exhibiting a Tb^{3+} and Eu^{3+} characteristic temperature-dependent luminescence with a high rate Tb^{3+} -to- Eu^{3+} energy transfer. According to theoretical calculations, the modifications of photoluminescence properties and the increase in the pairwise Tb^{3+} -to- Eu^{3+} energy transfer rate by about 10 times can be rationalized as a change of the coordination number of the Ln^{3+} sites of the complex from 7 to 8 accompanied by a symmetry evolution from C_s to C_{4v} and a slight shortening of intramolecular Ln^{3+} - Ln^{3+} distances upon the effect of encapsulation. These nanothermometers operate in the 20–70 °C range with excellent photothermal stability, cyclability and repeatability (>95%), displaying a maximum relative thermal sensitivity of 1.4% °C⁻¹ (at 42.7 °C) in water. Furthermore, they can operate in cells with a thermal sensitivity of 8.6% °C⁻¹ (at 40 °C), keeping in mind that adjusting the calibration for each system is necessary to ensure accurate measurements.

Received 21st April 2023,
Accepted 28th July 2023
DOI: 10.1039/d3nr01851b
rsc.li/nanoscale

Introduction

Precise temperature measurement at micro and nanoscales is of crucial importance for many applications from biology and medicine to cryogenics.^{1–3} In the last two decades, an attractive field of research based on the use of luminescent thermal probes has emerged, giving access to a wide temperature

measurement range, high accuracy, remote detection, fast response and high spatial resolution.¹ A plethora of luminescent nanothermometers based on trivalent lanthanide (Ln^{3+}) ions with their advantages and drawbacks have been reported.⁴ We can mention upconverting and downshifting nanoparticles,^{5–8} metal organic frameworks (MOFs),^{9–15} complexes,^{16,17} and hybrid materials.¹⁸ These probes provide accurate temperature measurements with a high spatial resolution below 10 μm and an impressive thermal resolution of 0.1 K. They achieve these measurements within a short acquisition time of less than 10 μs while exhibiting a high sensitivity of $S_r > 1\%$ °C⁻¹.^{19–23} However, an important number of them work in the solid state and their use in water and biological media remains relatively challenging. Note also that an effort has been made for remote and local temperature measurements in living cells,^{24–26} while the reliability of their intracellular thermal readout is still a question of debate.²⁷

^aICGM, Univ. Montpellier, CNRS, ENSCM, Montpellier, France.

E-mail: joulia.larionova@umontpellier.fr, yannick.guari@umontpellier.fr

^bIBMM, Univ. Montpellier, CNRS, ENSCM, Montpellier, France

^cDepartment of Biochemistry, Medical Research Institute, University of Alexandria, Alexandria, Egypt

^dDepartment of Physics and CICECO – Aveiro Institute of Materials, University of Aveiro, 3810-193 Aveiro, Portugal. E-mail: albanoneto@ua.pt, lcarlos@ua.pt

^eLaboratoire de Chimie, ENS de Lyon, Université de Lyon, Lyon, France

† Electronic supplementary information (ESI) available. See DOI: <https://doi.org/10.1039/d3nr01851b>



Ln^{3+} -based complexes have demonstrated their excellence as luminescence thermometry candidates. They exhibit unique photophysical properties, including long-lived emissions with lifetimes reaching the millisecond scale, specifically in the visible and/or infrared spectral regions. These properties stem from the 4f–4f transitions, contributing to narrow emission lines, significant Stokes shifts, and high quantum yields.^{28,29} Moreover, their photoluminescence features can easily be adjusted by playing on the choice of lanthanide ions and their coordination environment, as well as on the option of antenna ligands. Particular attention in recent years has been devoted to the design of ratiometric and self-calibrated nano-thermometers, where the luminescence intensity ratio (LIR) measured from two Ln^{3+} sites may be used for absolute measurements of temperature with high sensitivity and large temperature range tunability.²⁰ The mostly used couple of lanthanide ions is the $\text{Tb}^{3+}/\text{Eu}^{3+}$ system^{9,13,16} due to the high emission quantum yield generally typical of the ions for which different parameters can be optimized in order to increase the temperature sensor's performances. Thus, the distance between the two Ln^{3+} ions, the ratio between them, the nuclearity of the complexes, their structural organization and environment, and the nature of ligands govern the efficiency of the ion–ion (if operational) and ligand-to-ion energy (singlet and triplet ligand states) transfer mechanisms. However, Ln^{3+} complex-based thermometers can present several drawbacks: (i) chemical and optical instabilities happening all the more with increasing temperature;³⁰ (ii) insolubility and/or instability in water precluding any use for biomedical applications and temperature determination in catalytic, phase transition or enzymatic reactions occurring in aqueous media, and (iii) emission quenching through O–H and C–H group vibrations particularly in water.³¹ In order to overcome these problems, the incorporation of these complexes in protective hosts formed using polymers or organic–inorganic matrixes has been investigated.²⁰

In this line of thought, numerous solid-state hybrid thermometers have recently been developed based on various Ln^{3+} -based complexes inserted into optically transparent polymer nanoparticles,^{32–34} organosilica nanoparticles^{35,36} or in the shells of hybrid core–shell nanoparticles.^{37,38} However, only a limited number of these probes have been tested in water, and even fewer have been examined in biological systems.³⁹ Notably, there is an important lack of investigations exploring the behavior of these thermometers in various media/systems, highlighting the need for further research to assess their response in different environments.

Additionally, the impact of the hosting matrix on the temperature-dependent emission mechanism has received only limited attention.^{20,32}

Despite the advantages of mesostructured silica nanoparticles as porous matrices, there is a notable scarcity of reports on their utilization as nano-hosts for designing emissive nanothermometers. To the best of our knowledge, only one work has focused on incorporating organic dyes within these nanoparticles, demonstrating a good thermal sensitivity ($S_r \sim 1\% \text{ } ^\circ\text{C}^{-1}$) in water within the temperature range of

20–50 $^\circ\text{C}$.⁴⁰ While lanthanide ion complexes have been incorporated into mesostructured silica nanoparticles for imaging and labeling applications, their use for designing luminescent thermometers has not been explored.^{41–46}

In this work, we explore the potential of mesostructured silica nanoparticles (MSN) having a stellate morphology incorporating host β -diketonate Ln^{3+} complexes as photostable ratiometric thermometers in water, in PBS or in cells. Both synthetic phosphate buffered saline (PBS) in the 20–70 $^\circ\text{C}$ temperature range and living cells, between 20 and 40 $^\circ\text{C}$, were tested. The choice of the stellate MSN was based on: (i) a largely tunable and open porosity with the pore size ranging from *ca.* 10–20 nm compatible with functional species with relatively large size functions (such as complexes, biomolecules, or enzymes), (ii) a tunable particle size in the range of 50–400 nm, (iii) a unique open pore structure, and (iv) the possibility to functionalize their internal and external surfaces by co-condensation approaches.^{47,48} Recently, we reported on a dual functionalization of MSN with both 1,4-pyridine on the internal surface employed for the efficient immobilization of a bio-inspired catalytically active $\{[\text{Mn}(\text{bpy})(\text{H}_2\text{O})](\mu\text{-}2\text{-MeC}_6\text{H}_4\text{COO})_2(\mu\text{-O})\}[\text{Mn}(\text{bpy})(\text{NO}_3)]\text{NO}_3$ complex on one hand and with the sulfobetaine zwitterion on the external surface to ensure high colloidal stability of nano-objects on the other hand.⁴⁹ In this work, we extend our approach to the encapsulation of a luminescent $[(\text{Tb}/\text{Eu})_9(\text{acac})_{16}(\mu_3\text{-OH})_8(\mu_4\text{-O})(\mu_4\text{-OH})]$ (acac = acetylacetonate) complex into dually functionalized MSN with the acetylacetonate moieties anchored into the pores and the sulfobetaine zwitterion grafted on the external surface. This $\text{Tb}^{3+}/\text{Eu}^{3+}$ complex has been chosen due to the good photoluminescence properties of its constituent Ln^{3+} ions and its photothermal stability in the solid state,^{50,51} while its thermometric ability has never been reported until now. Note that it may be considered as a “lanthanide molecular cluster” with promising photo-luminescence properties.⁵² Its high nuclearity ensures a rigorous co-localization of both luminescent probes (Tb^{3+} and Eu^{3+}) in the silica pores and optimized conditions for correlation with local temperature measurement. Additionally, this configuration offers the advantage of controlling the $\text{Tb}^{3+}/\text{Eu}^{3+}$ ratio, which is not feasible with the separate use of Eu and Tb mononuclear complexes. The use of different $\text{Tb}^{3+}/\text{Eu}^{3+}$ ratios (such as 9/1 and 19/1) allowed the LIR of the respective Ln^{3+} emissions to vary, providing self-referencing emissive systems, in which the temperature sensor's performances can be optimized.³² Furthermore, the acac ligand provides not only the antenna effect, but also the advantage to be easily covalently incorporated into mesoporous silica as we shall see below. After the post-synthetic clogging of the silica pores, we obtained hybrid nanoparticles of *ca.* 90 nm, presenting characteristic Tb^{3+} and Eu^{3+} emissions in water with a higher Tb^{3+} to Eu^{3+} energy transfer rate in comparison with the parent free complexes. Note also that the latter cannot be used as luminescent thermometers in water due to their poor solubility and stability. The temperature dependence of the emission permitted us to use these nanoparticles as temperature nanoprobe



working in water, in PBS and in cells with high sensitivity (up to 1.4% °C⁻¹ at 42.7 °C in water and 8.64% °C⁻¹ in cells) and high thermo- and photostabilities.

Experimental

General procedures

Tetraethoxysilane (TEOS) was purchased from ABCR (Karlsruhe, Germany), hexadecyltrimethylammonium *p*-toluenesulfonate (CTATos), ethanol and acetonitrile were purchased from Merck (Darmstadt, Germany), 3-((dimethyl(3-trimethoxysilyl)propyl)-ammonio)propane-1-sulfonate (SBS) was purchased from Gelest (Morrisville, NC, USA), ammonium nitrate, triethanolamine (TEAH₃), terbium(III) chloride hexahydrate and europium(III) chloride hexahydrate were purchased from Sigma-Aldrich (Steinheim, Germany), and 2-4-pentanedione (Hacac) was purchased from Alfa Aesar (Haverhill, USA). 3-[3-(Triethoxysilyl)propyl]pentane-2,4-dione (acac-Si) was synthesized according to the protocol described by B. Yuan *et al.* in 2011.⁵³

All culture media, antibiotics and FBS were purchased from ThermoFisher scientific, USA.

Synthesis

Synthesis of mixed Tb³⁺/Eu³⁺ complexes (compounds 1 and 2). The synthesis of lanthanide mixed compounds [(Tb/Eu)₉(acac)₁₆(μ₃-OH)₈(μ₄-O)(μ₄-OH)]·H₂O, where Tb/Eu ratio = 19/1 (1) and 9/1 (2), was performed in the same manner as in the previously published procedure for Tb³⁺-based analogues.⁵⁰ For this, 1 mmol TbCl₃·6H₂O and EuCl₃·6H₂O and 2 mmol Hacac were dissolved in 3 mL of methanol and then 4 mmol triethylamine were added slowly to the solution. Colorless crystals were obtained when the solutions were kept at 4 °C for one night.

Compound 1. EDS: Tb/Eu = 18.5/1. The IR spectrum is shown Fig. S1 (ESI[†]), elemental analysis: calculated (%) C (29.9), H (4.3); found (%) C (30.3), H (4.1), the powder XRD pattern is coherent with the previously reported Tb³⁺ compound (Fig. S2 (ESI[†])).⁵⁰

Compound 2. EDS: Tb/Eu = 9.3/1. The IR spectrum is shown Fig. S1 (ESI[†]), elemental analysis: calculated (%) C (29.9), H (4.3); found (%) C (30.2), H (4.2), the powder XRD pattern is coherent with the previously reported Tb³⁺ compound (Fig. S2 (ESI[†])).⁵⁰

Synthesis of MSN functionalized with acac and sulfobetaine zwitterion (sample MSN). 0.96 g of hexadecyltrimethylammonium *p*-toluenesulfonate (CTATos) and 0.19 g of triethanolamine (TEAH₃) were dissolved in 50 mL of ultrapure water and heated at 80 °C for one hour under magnetic stirring at 500 rpm. 0.74 g (2.4 mmol) of 3-[3-(triethoxysilyl)propyl]pentane-2,4-dione (acac-Si) and 6.50 g (31.2 mmol) of TEOS were then added into the solution and vigorously stirred for 2 h at 80 °C. For functionalization with the zwitterion, 0.50 g of 3-((dimethyl(3-trimethoxysilyl)propyl)-ammonio)propane-1-sulfonate (SBS) was added after 2 h and stirred at 80 °C overnight. At the end of the reaction, the solution was cooled down

at room temperature and the nanoparticles were collected by centrifugation at 20 krpm for 10 min. The surfactant CTATos was extracted by three washings of 30 min each in an ethanolic solution of ammonium nitrate at 6 g L⁻¹ using an ultrasonic bath. The nanoparticles were then washed three times with water and one time with ethanol and dried overnight at 80 °C in an oven.

IR (ATR): δ(Si-O-Si) = 460 cm⁻¹ (SiO₂), ν(Si-O-Si) = 980–1250 cm⁻¹ (SiO₂), ν(C=C) = 1350–1400 cm⁻¹ (acac-Si), ν(C-N) = 1485 cm⁻¹ (SBS), ν(C=O) = 1700 cm⁻¹ (acac-Si), ν(C-H) = 2900–3000 cm⁻¹ (acac-Si); elemental analysis found (%): C(12.8), H(2.6), N(0.5), S(0.8); EDS: Si/S = 97.75/2.25; estimated formula (M): (SiO₂)₁(CTA)_{0.010}(acac-Si)_{0.064}(SBS)_{0.021} (79.8 g mol⁻¹); nitrogen sorption: S_{BET} = 344 m² g⁻¹; d_{TEM} = 92.9 ± 8.4 nm; δ¹³C (ss-NMR): CH₂ of acac (12.7 ppm, 21.3 ppm), carbon signals of SBS (29.9 ppm, 43.3 ppm, 47.8 ppm, 51.4 ppm, 53.8 ppm), CH of acac (67.9 ppm), quaternary C of acac (111.0 ppm), C=O & C-O of acac (192.2 ppm, 206.8 ppm); δ²⁹Si (ss-NMR): -59 ppm (T₂), -67 ppm (T₃), -91 ppm (Q₂), -102 ppm (Q₃), -110 ppm (Q₄).

Encapsulation of lanthanide complexes 1 and 2 into functionalized MSN (samples MSN-1, MSN-2). 10 mg of nanoparticles (MSN) and 2.4 μmol (4.6 mg) of 1 or 2 for the synthesis of MSN-1 or MSN-2, respectively, were dispersed in 10 mL of MeOH and kept under stirring at 500 rpm and 60 °C for 2 hours. The nanoparticles were collected by centrifugation at 20 krpm for 15 min and washed once with MeOH and twice with water.

To clog the pores, 10 mg of loaded nanoparticles were dispersed in 6 mL of water. Under stirring at 500 rpm and at 60 °C, 60 μL of TEOS were added to the suspension. The pH of the suspension was adjusted at around 9 with a solution of NaOH at 1 M. The suspension was left under stirring and heating for one night. The nanoparticles were collected by centrifugation at 20 krpm for 15 min and washed three times with water and dried at 60 °C in an oven. Before their use in water for measurements, the samples were thermally treated for one hour at 70 °C.

Characterization of MSN-1. IR (ATR): δ(Si-O-Si) = 460 cm⁻¹ (SiO₂), ν(Si-O-Si) = 980–1250 cm⁻¹ (SiO₂), ν(C=C) = 1350–1400 cm⁻¹ (acac-Si, 1), ν(C-N) = 1485 cm⁻¹ (SBS), ν(C=O) = 1510 cm⁻¹ (1), ν(C=O) = 1700 cm⁻¹ (acac-Si), ν(C-H) = 2900–3000 cm⁻¹ (acac-Si, 1). S_{BET} = 286 m² g⁻¹; d_{TEM} = 95.0 ± 9.7 nm.

Elemental analysis found (%): C(5.8), H(1.9), N(0.2), S(0.1); EDS: Si/Tb = 26.7/1; ICP: Tb/Eu = 20.8.

Estimated formula: (SiO₂)₁(CTA)_{0.0017}(acac-Si)_{0.0074}(SBS)_{0.0024}(1)_{0.0047}.

Characterization of MSN-2. IR (ATR): δ(Si-O-Si) = 460 cm⁻¹ (SiO₂), ν(Si-O-Si) = 980–1250 cm⁻¹ (SiO₂), ν(C=C) = 1350–1400 cm⁻¹ (acac-Si, Ln(acac)₃), ν(C-N) = 1485 cm⁻¹ (SBS), ν(C=O) = 1510 cm⁻¹ (2), ν(C=O) = 1700 cm⁻¹ (acac-Si), ν(C-H) = 2900–3000 cm⁻¹ (acac-Si, 2). S_{BET} = 307 m² g⁻¹; d_{TEM} = 93.2 ± 7.1 nm.

Elemental analysis found (%): C(6.7), H(2.1), N(0.2), S(0.2); EDS: Si/Tb = 30.1/1; ICP: Tb/Eu = 9.1/1.



Estimated formula: $(\text{SiO}_2)_1(\text{CTA})_{0.004}(\text{acac-Si})_{0.024}(\text{SBS})_{0.008}(\text{2})_{0.0038}$.

Complexes' leaching experiments. The MSN-1 or MSN-2 (~3 mg) nanoparticles were dispersed in water for several hours under stirring. Then, they were removed by centrifugation and photoluminescence spectra were recorded for the remaining solutions. The excitation and emission spectra were flat and did not show the characteristic bands of complexes, proving that the complexes remain confined in the silica nanoparticles.

Methods

Transmission electron microscopy (TEM) images were recorded at 100 kV (JEOL 1200 EXII). Samples for TEM measurements were deposited from suspensions on copper grids and allowed to dry before observation. The size distribution histograms were determined using enlarged TEM micrographs taken at a magnification of 100 K on a statistical sample of *ca.* 100 nanoparticles. SEM/EDS microscopy was performed on an FEI Quanta FEG 200 instrument. The powders were deposited on an adhesive carbon film and analyzed under high vacuum. The quantification of heavy elements was carried out using Oxford Instruments AZTEC software, with a dwell time of 3 μs . HRTEM and STEM-EDS measurements were performed on a JEOL 2200 FS microscope and an Oxford Instruments SDD EDX detector XMaxN 100 TLE (100 mm^2 – windowless). Hydrodynamic diameter measurements were performed on Malvern nanoseries, Zetasizer NanoZS (Model ZEN3600) in a DTS1060C Zetacell (for the zeta potential) in water at 25 °C with an equilibration time of 120 s with automatic measurement and the data were treated with Zetasizer software using a Smoluchowski model. Thermogravimetric analysis (TGA) was performed using a Netsch STA 409 PC analyser in the 20–1100 °C temperature range at a heating speed of 5 °C min^{-1} under air. The composition of the nanoparticles was determined by elemental analysis (C, H, N, S) and the amount of Si was calculated based on the TGA results by considering the resulting mass at 1100 °C as pure SiO_2 . Elemental analyses were performed with an Elementar Vario Micro Cube analyzer. Powders were pyrolyzed at 1150 °C and then reduced at 850 °C over hot copper. Gases were separated by gas chromatography. ICP-AES analysis was performed by using a Spectro Arcos ICP (AMETEK Materials Analysis). The samples were digested in 10 M NaOH before being diluted to obtain 10 mL of a final solution in 1% HNO_3 . Infrared spectra were recorded as KBr disks (1 wt% of sample) on a PerkinElmer Spectrum Two spectrophotometer with four acquisitions at a resolution of 4 cm^{-1} . Nitrogen adsorption and desorption isotherms at 77 K were measured using a TriStar 3000 (V6.06 A). Prior to the sorption experiment, the samples were dried under vacuum at 80 °C for 12 h. The specific surface area (S_{BET}) was calculated according to the Brunauer–Emmett–Teller (BET) method. Pore size distribution was obtained from the desorption branch of the nitrogen isotherm using the Barrett–Joyner–Halenda (BJH) equation. All solid-state NMR experiments were performed on a Varian VNMRs 300 MHz (7.05 T) NMR spectrometer. A

3.2 mm Varian T3 HXY magic angle spinning (MAS) probe was used for ^{13}C and ^{29}Si experiments, at operating frequencies of 599.82 and 564.33 MHz, respectively. ^1H – ^{13}C CPMAS NMR spectra were recorded by spinning at 5 kHz, with a contact time of 2.5 ms and 300 kHz, and ^1H decoupling during acquisition. 15 000 scans were recorded for ^{13}C experiment and 4000 scans for ^{29}Si experiment. ^{13}C chemical shifts were referenced externally to adamantane (used as a secondary reference), with the high-frequency peak being set to 38.5 ppm.

Photoluminescence measurements

Emission and excitation spectra were measured at room (298 K) in the solid state and at low (77 K) temperatures, as well as in water, PBS solution or cell medium using a spectrofluorimeter Edinburgh FLS-920. The excitation source was a 450 W Xe arc lamp. The spectra were corrected for the detection and optical spectral response of the spectrofluorimeter.

Photoluminescent measurements as a function of temperature were performed by using the temperature setup incorporated into the Edinburgh spectrofluorimeter. Measurements in liquids (water, PBS, cells medium) were performed using solutions of 1 mg mL^{-1} nanoparticles under continuous stirring. Emission spectra were recorded in the temperature range from 20 to 70 °C for water and PBS and between 20 and 40 °C for cells. At each temperature step, a period of 2 min was given to allow the temperature to stabilize, and then 5 emission spectra were recorded with a dwell time of 0.3 s and a step of 1 nm.

Cell lines

Human breast adenocarcinoma (MCF-7) and human retinoblastoma (Y-79) cell lines purchased from American Type Culture Collection (ATCC) were used in this study. The MCF-7 cells were maintained in Dulbecco's modified Eagle's medium with nutrient mixture F-12 Ham (DMEM/F-12) supplemented with 10% fetal bovine serum (FBS) and 1% penicillin/streptomycin (P/S). The Y-79 cells were maintained in Roswell Park Memorial Institute (RPMI) 1640 medium supplemented with 20% FBS and 1% P/S. Cell lines were maintained under a humidified atmosphere with 5% CO_2 at 37 °C in a HERACell™ 150 incubator (Thermo Fisher Scientific, France).

Cytotoxicity

Human MCF-7 cell lines were seeded in a 96-well plate at a density of 5000 cells per well and left to incubate for 24 h. Then, the cells were treated with different concentrations of MSN-1 (previously thermally treated for one hour at 70 °C) ranging between 0 and 200 $\mu\text{g mL}^{-1}$. Control cells were treated with the vehicle. After 3 days of incubation with nanoparticles, cell viability was assessed using the colorimetric 3-(4,5-dimethylthiazol-2-yl)-2,5-diphenyltetrazolium bromide (MTT) assay. In this assay, the yellow soluble MTT solution was added to the cells at a final concentration of 0.5 mg mL^{-1} , followed by 4 h of incubation at 37 °C. After the incubation period, the medium was aspirated and the insoluble violet formazan crystals were solubilized with a mixture of dimethyl sulfoxide and ethanol (1:1, v/v), followed by 20 min of



shaking. The absorbance was measured at 540 nm and the intensity of the violet colour is directly proportional to the viable cells. The cell viability percentage was calculated as $(Ab_{\text{test}}/Ab_{\text{control}}) \times 100\%$. The experiment was performed 2 times in quadruplicate.

Nanoparticle uptake in cells

Human MCF-7 cell lines were seeded on cover glasses (20 mm \varnothing) and left to incubate for 24 h. Afterwards, the cells were treated with $100 \mu\text{g mL}^{-1}$ **MSN-1** then left to incubate for another 24 h. After the end of the incubation period, the cells were washed 3 times with PBS, and then were fixed with 2.5% (v/v) of glutaraldehyde in 0.1 M sodium cacodylate buffer at 4 °C. Samples were post-fixed with 1% osmium tetroxide, dehydrated by a graded series of alcohols, placed in a 1 : 1 mixture of absolute ethanol and Epon 812 and changed to fresh resin twice. All these steps were performed using Pelco BioWave Pro+. Samples were placed upside-down upon Eppendorf caps full of fresh resin and placed in a 65 °C oven and partially polymerized. Then, the samples were separated from the Eppendorf caps by immersing them in liquid nitrogen. Afterwards, the Epon blocks were sectioned on an ultramicrotome (UC7 Leica). The obtained ultra-thin sections of 70 nm were mounted on 100-mesh collodion-coated copper grids (stained with uranyl acetate and lead citrate), and finally observed with a JEOL 1400Plus electron microscope.

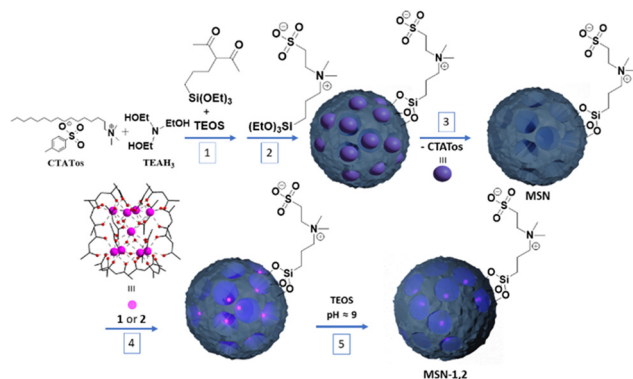
Thermometry measurements in cells

Human Y-79 cell line were seeded in two 25 cm² cell culture flasks (T25), one flask served as a control and the other flask was treated with $100 \mu\text{g mL}^{-1}$ **MSN-1** for 24 h. Then, 10^6 cells were sampled from each flask and centrifuged at 1300 rpm for 5 min at 4 °C. The supernatants were aspirated and the cell pellets were suspended in PBS and kept in ice until the measurement. Luminescence and thermometry measurements were performed under similar conditions to the ones on **MSN-1** in water. Photoluminescence measurements as a function of temperature were performed by using the temperature setup incorporated into the Edinburgh spectrofluorimeter. Measurements were performed on the cells dispersed in 1.5 mL of PBS. Emission spectra were recorded in the reduced temperature range from 20 to 40 °C every 2 °C and in a reduced spectral range from 530 to 640 nm. At each temperature step, a period of 2 min was given to allow the temperature to stabilize, and then 10 emission spectra were recorded with a dwell time of 0.3 s and a step of 1 nm.

Results and discussion

Synthesis

The design of luminescent MSN loaded with mixed Tb³⁺/Eu³⁺ complexes **1** and **2** inside the porosity of dually functionalized mesostructured silica has been performed by using a two-step procedure depicted in Scheme 1. First, the functionalized **MSN** nanoparticles containing acac moieties anchored inside the



Scheme 1 Schematic representation of the synthesis of functionalized hybrid nanoparticles **MSN-1** and **MSN-2**. The used complexes **1** or **2** are $[(\text{Tb}/\text{Eu})_9(\text{acac})_{16}(\mu_3\text{-OH})_8(\mu_4\text{-O})(\mu_4\text{-OH})]\cdot\text{H}_2\text{O}$ (where Tb/Eu ratio = 19/1 for **1** and 9/1 for **2**).

pores and sulfobetaine zwitterion on the nanoparticles' surface were synthesized by a sol-gel process using hexadecyltrimethylammonium *p*-toluenesulfonate (CTATos) as a surfactant and triethanolamine (TEAH₃) as a basic catalyst. The functionalization of MSN was performed *in situ* first by the co-condensation procedure during the sol-gel reaction by adding acac-siloxane and TEOS for its preferential grafting within the nanoparticles, followed by a delayed co-condensation with zwitterionic sulfobetaine siloxane to provide its preferential grafting at the surface of the nanoparticles, as the pores were obstructed by the surfactant. This latter was then removed by thorough washing, which liberated the silica porosity and permitted the acetylacetonate groups' accessibility (see Table 1 for characteristics of **MSN** samples).

Second, the mixed $[(\text{Tb}/\text{Eu})_9(\text{acac})_{16}(\mu_3\text{-OH})_8(\mu_4\text{-O})(\mu_4\text{-OH})]\cdot\text{H}_2\text{O}$ compounds (where Tb/Eu ratio = 19/1 for **1** and 9/1 for **2**) were then incorporated into the silica pores by their impregnation in methanol for 2 h under slight heating. Then the pores were clogged by using TEOS in order to avoid the leaching of complexes and any chemical interaction with their environment providing samples **MSN-1** and **MSN-2** (Scheme 1). Therefore, the obtained nanoparticles contain incorporated mixed Tb³⁺/Eu³⁺ complexes inside the closed pores assuring the targeted luminescence and zwitterion on the surface of the nanoparticles, providing colloidal stability. Elemental (C, H, N, S) and EDS (Si, Tb and Eu) analyses provided the estimated formula for samples **MSN** and **MSN-1** and **MSN-2**, which settle the functionalization of MSN with acetylacetonate and the zwitterion in one hand and confirm the presence of lanthanide complexes **1** and **2** inside the pores on the other hand (see the Experimental section). Loading up to 0.0047 and 0.0038 units of complexes **1** and **2** per unit of SiO₂ for **MSN-1** and **MSN-2**, respectively, was observed (*i.e.*, 0.042 or 0.034 units of lanthanides per unit of SiO₂ for **MSN-1** and **MSN-2**, respectively). Note that a similar loading capacity (0.053 units of complex per unit of SiO₂) was previously obtained for the $[\{\text{Mn}(\text{bpy})(\text{H}_2\text{O})\}(\mu\text{-2-MeC}_6\text{H}_4\text{COO})_2(\mu\text{-O})\{\text{Mn}(\text{bpy})(\text{NO}_3)\}]\text{NO}_3$ complex in our previous work.⁴⁹ The loss in



Table 1 Some characteristics of samples **MSN**, **MSN-1** and **MSN-2**

Sample	Composition ^a	S_{BET} (m ² g ⁻¹)	d_{TEM} (nm)
MSN	(SiO ₂) ₁ (CTA) _{0.010} (acac-Si) _{0.064} (SBS) _{0.021}	344	92.9 ± 8.4
MSN-1	(SiO ₂) ₁ (CTA) _{0.0017} (acac-Si) _{0.0074} (SBS) _{0.0024} (1) _{0.0047}	286	95.0 ± 9.7
MSN-2	(SiO ₂) ₁ (CTA) _{0.004} (acac-Si) _{0.024} (SBS) _{0.008} (2) _{0.0038}	307	93.2 ± 7.1

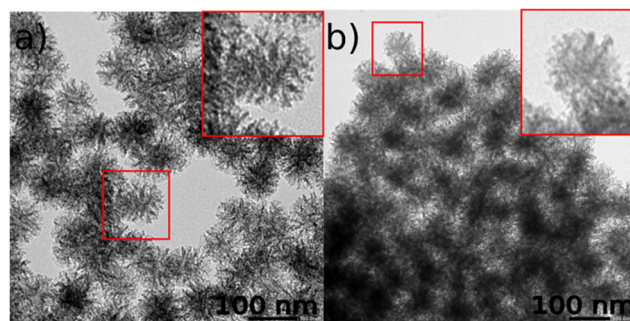
^a Calculated from the elemental and EDS analyses.

the amount of C for **MSN-1** and **MSN-2** when compared to **MSN** is easily explained by the clogging step during which the number of SiO₂ units is increased.

Infrared (IR) spectroscopy allowed us to confirm first the grafting of the acetylacetonate and sulfobetaine zwitterion moieties on the internal and external surfaces of **MSN** and second to ensure the presence of lanthanide complexes inside the silica nanoparticles (Fig. S1, ESI†). First, Fig. S1a and b† show the comparative IR spectra of pristine and loaded silica nanoparticles, where all of them demonstrate the presence of the C–H vibrational bands between 2900 and 3000 cm⁻¹, the characteristics bands of silica ($\nu(\text{Si–O–Si}) = 1080 \text{ cm}^{-1}$, $\nu(\text{Si–OH}) = 952 \text{ cm}^{-1}$, $\nu(\text{Si–O–Si}) = 805 \text{ cm}^{-1}$, and $\delta(\text{Si–O–Si}) = 460 \text{ cm}^{-1}$), as well as the bands from the grafted acetylacetonate ($\nu(\text{C=O}) = 1700 \text{ cm}^{-1}$ and $\nu(\text{C=C}) = 1350\text{--}1400 \text{ cm}^{-1}$ in the enol form) and the zwitterion ($\nu(\text{C–NH}) = 725 \text{ cm}^{-1}$), proving the presence of organic functionalities grafted in/on the silica nanoparticles.⁵⁴ Second, the IR spectra of **MSN-1** and **MSN-2** demonstrate: (i) an important increase in the $\nu(\text{C–H})$ signal of acac between 2900 and 3000 cm⁻¹ in comparison with the one of **MSN** (Fig. S1a, ESI†), (ii) the appearance of bands at 1620 and 1613 cm⁻¹, and 1389 and 1381 cm⁻¹ that are presented in the IR spectra of **1** and **2** (Fig. S1c, ESI†), and which are absent for **MSN** (Fig. S1d, ESI†);⁵⁰ note, however, that their position is slightly shifted (*ca.* 7–9 cm⁻¹) towards higher wavenumbers in comparison with the original bands of the complexes, and (iii) the relative intensity of the band at 1700 cm⁻¹ in **MSN-1** and **MSN-2** attributed to the $\nu(\text{C=O})$ of the free acac ligand decreases in comparison with the IR spectrum of **MSN** (Fig. S1d, ESI†). Therefore, these results confirm the presence of complexes **1** and **2** in the silica nanoparticles. The modifications (bands shift towards higher wavenumbers and modification of their relative intensity) observed in the IR spectra of the encapsulated compounds into the nanoparticles may be attributed to both the occurrence of weak interactions between the complexes and the silica nanoparticles and/or the coordination of grafted silica pores of the acac ligands to lanthanide ions through the ligand exchange.

The grafting of acetylacetone and the zwitterion on the internal and external porosities of silica nanoparticles was also confirmed by using solid-state ²⁹Si and ¹³C NMR. The former spectrum shows the presence of *T*₂ and *T*₃ signals at –59 ppm and –69 ppm, respectively, confirming the grafting of organosilanes (SBS and acac-Si in Fig. S3, ESI†). The ¹³C solid-state NMR spectrum (Fig. S4, ESI†) exhibits the carbon signals previously described for the SBS zwitterion, with the carbon

signal in the α position of the sulfonate group at 49 ppm and the other methylene carbons of the alkane chain as a broad peak at 15 ppm, confirming the presence of the zwitterion denoted as SBS in the spectrum. The signal expected around 61 ppm from the carbon at the α position of the nitrogen from the ammonium cannot be observed as there is an intense broad signal from the acac group at this chemical shift. As there is an equilibrium between the keto and enol forms of the acetylacetonate function, a multiplication of the signals was observed. The unshielded ¹³C signals of the carbons in the α position of the carboxylate (denoted as 4 and 4' in Fig. S4†) or the enol (denoted as 4') can be easily identified at 210 ppm and 193 ppm, respectively, and the one for the enol at 110 ppm (denoted as 3'). The remaining aliphatic carbons from both forms have similar signals at 22 ppm (denoted as 5, 5', 5'') and 16 ppm (denoted as 1, 2). Note that the peaks at 30, 33 and 54 ppm are due to residual CTA. Therefore, the characteristic peaks for both the acac and zwitterion functions were clearly identified by NMR, which confirms the expected functionalization of **MSN**. The NMR characterisation of samples **MSN-1** and **MSN-2** cannot be performed due to the paramagnetic character of Tb³⁺ in the lanthanide complexes. Transmission electronic microscopy (TEM) images demonstrate that functionalized nanoparticles **MSN** exhibit a stellate-like shape with an open and radial porosity and have a size of 92.9 ± 8.4 nm (Fig. 1a). The introduction of Tb³⁺/Eu³⁺ compounds **1** and **2** followed by pore clogging seems to bring no major changes in the size (Fig. 1b and Fig. S5, ESI†). The mean size of samples **MSN-1** and **MSN-2** is equal to 95.0 ± 9.7 and 93.2 ± 7.1 nm, respectively, which is quite close to the one of the initial **MSN**. However, we can note a slight modification

**Fig. 1** TEM images of: (a) pristine functionalized **MSN** and (b) **MSN-1**.

of the porosity, which seems to be more obstructed, suggesting a successful incorporation of the complexes and pore clogging.

The obtained nanoparticles **MSN-2** have also been characterized by HAADF-STEM with EDS mapping, which allowed to visualize the homogeneity of the atomic distribution of sulfur from the sulfobetaine zwitterion and terbium atoms, confirming the encapsulation of the $\text{Tb}^{3+}/\text{Eu}^{3+}$ complex (Fig. 2). We can also observe an intense signal from the C atoms due to the acetylactonate functions grafted onto the silica and the ones from the loaded compounds. Note that the Eu atoms are difficult to visualize by this technique due to their very low amount. This situation has already been described in other work.³⁹

Nitrogen sorption measurements performed on functionalized empty silica nanoparticles (**MSN**) and samples **MSN-1** and **MSN-2** permit to estimate the impact of the $\text{Tb}^{3+}/\text{Eu}^{3+}$ compound encapsulation and pore clogging on the pore size and specific surface area (Fig. S6, ESI†). As observed by TEM, empty **MSN** possess a stellate-like morphology with an open porosity, presenting a pore size of 15 nm and a high specific surface area of $344 \text{ m}^2 \text{ g}^{-1}$ (Table 1). These data are coherent with the double-functionalized stellate-like nanoparticles.⁴⁹ The specific surface area decreases after encapsulation of **1** and **2** and pore clogging goes from 344 to 286 and $307 \text{ m}^2 \text{ g}^{-1}$ for **MSN-1** and **MSN-2**, respectively (Table 1).

The positive effect of the zwitterions grafted on the nanoparticles' surface on colloidal stability was previously reported.^{49,55} The colloidal stability of **MSN-1** at 0.1 mg mL^{-1} in water or a mixture of 10% fetal bovine serum and 90% high glucose (DMEM) was investigated by DLS over 48 hours (Fig. S7, ESI†). In water, a short increase in the hydrodynamic diameter was observed after 3 hours (130 to 160 nm) before

stabilizing around 200 nm for the following 40 hours. The presence of a layer of grafted zwitterions, along with the associated counter ions interacting with the charged groups in solution, explains the fact that the hydrodynamic diameter weighted in intensity observed by DLS appeared larger than the size of the silica nanoparticles determined by TEM. Additionally, the influence of solvent molecules bonded to the zwitterion layer should be taken into account. The decrease in scattered intensity is associated with the increase of the hydrodynamic diameter, which is observed within the first hours (Fig. S7c†), followed by stabilization after approximately 10 hours, indicating a process of nanoparticle aggregation and settling in water. After 10 hours, the scattered light intensity remains relatively constant, indicating that the nanoparticles have reached a state of equilibrium. In the protein rich media, we observed the formation of a corona in the first hour, leading to a fast increase in diameter from 200 to 250 before stabilizing without any aggregation observed for the following 24 h hours. In contrast, the non-functionalized nanoparticles rapidly aggregate.⁴⁹ Moreover, complex loading followed by pore clogging did not affect the colloidal stability of the nanoparticles brought by the zwitterion situated on the external surface.⁴⁹

Photoluminescence properties

The photoluminescence of samples **MSN-1** and **MSN-2** was investigated in the solid state at 77 K and at room temperature in order to compare them with the ones of the parent complexes **1** and **2**, as well as in water and PBS in the temperature range of 20–70 °C to demonstrate the potential of the nanoparticles as luminescent temperature sensors.

The excitation spectra of **MSN-1** and **MSN-2** in the solid state at 77 K and at room temperature were recorded by monitoring both the main emissions of Eu^{3+} at 615 nm ($^5\text{D}_0 \rightarrow ^7\text{F}_2$) and Tb^{3+} at 550 nm ($^5\text{D}_4 \rightarrow ^7\text{F}_5$) (Fig. 3a, Fig. S8 and S9a–S12a, ESI†). They are dominated by a large broad band with a maximum at 326 and 325 nm (at 77 K) for **MSN-1** and **MSN-2**, respectively, attributed to the acac ligand excited states, indicating the advantage of excitation through antenna sensitization. The low intensities of the 4f transitions of both lanthanides can also be observed in these spectra depending on the monitored emission wavelength. In particular, the Tb^{3+} characteristic transitions appear when the spectra are recorded by monitoring the main emission of Eu^{3+} at 615 nm. In comparison, the excitation spectra of the parent $[(\text{Tb}/\text{Eu})_9(\text{acac})_{16}(\mu_3\text{-OH})_8(\mu_4\text{-O})(\mu_4\text{-OH})]\cdot\text{H}_2\text{O}$ compounds **1** and **2** measured at 77 K and at room temperature in the solid state (Fig. S13a–16a, ESI†) exhibit relatively pronounced 4f transitions beside the large broad band from 250 to 330 nm of acetylactonate-linked sensitization. This fact suggests that the acetylactonate-functionalized silica matrix provides a supplementary antenna effect, indeed improving the excitation through antenna ligand/host sensitization.

The emission spectra of **MSN-1** and **MSN-2** were recorded at 77 K and at room temperature in the solid state upon excitation through acetylactonate-linked sensitization (328 nm in

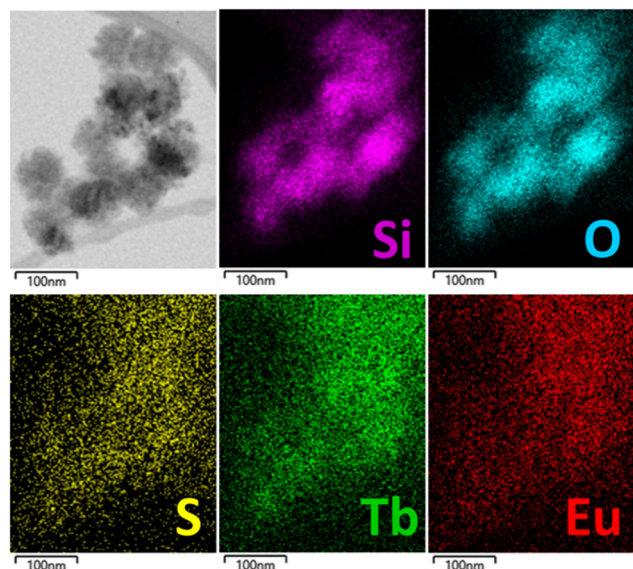


Fig. 2 STEM-bright field image and STEM-EDS elemental mapping of **MSN-2** with the topochemical distribution of Si (pink), O (cyan), S (yellow), Tb (green) and Eu (red).



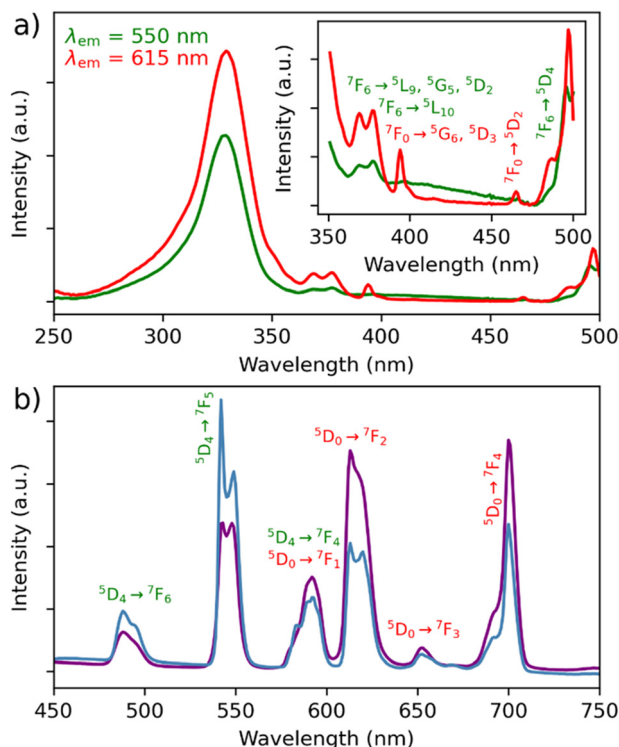


Fig. 3 (a) Excitation spectra of **MSN-1** monitored at $\lambda_{\text{em}} = 550$ (green) and $\lambda_{\text{em}} = 615$ nm (red) recorded in the solid state at RT. Inset: magnification of the excitation spectra between 340 and 510 nm. (b) Emission spectra of **MSN-1** recorded at 77 K (blue) and room temperature (violet) in the solid state with excitation at $\lambda_{\text{em}} = 328$ nm. Eu^{3+} and Tb^{3+} -linked transitions are shown in red and green, respectively.

the solid state), which are operational for both lanthanide ions since the wavelength corresponds to the maximum in the excitation spectra (Fig. 3b and Fig. S9b–S12b, ESI†). They exhibit:

(i) a series of classical $\text{Tb}^{3+} {}^5\text{D}_4 \rightarrow {}^7\text{F}_{6-0}$ characteristic emission lines (labelled in green) with the most intense ${}^5\text{D}_4 \rightarrow {}^7\text{F}_5$ transition;

(ii) a series of $\text{Eu}^{3+} {}^5\text{D}_0 \rightarrow {}^7\text{F}_{0-4}$ characteristic transitions (labelled in red) with the most intense band located at ca. 700 nm (${}^5\text{D}_0 \rightarrow {}^7\text{F}_4$). The higher intensity of the ${}^5\text{D}_0 \rightarrow {}^7\text{F}_4$ transition in comparison with the one observed in the spectra of the pristine complexes **1** and **2** (Fig. S13–S16, ESI†) indicates the important changes in the symmetry of the Eu^{3+} sites of the compounds inside the silica hosts,⁵⁶ which could be induced by the geometry modification, the coordination of acetylacetonate ligands of the silica host and/or by weak interactions between the encapsulated compound and the functionalized host matrix;

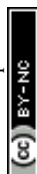
(iii) the relative intensity of the main $\text{Tb}^{3+} {}^5\text{D}_4 \rightarrow {}^7\text{F}_{6-0}$ transition dramatically decreases, while the intensities of two main Eu^{3+} characteristic transitions (${}^5\text{D}_0 \rightarrow {}^7\text{F}_2$ and ${}^5\text{D}_0 \rightarrow {}^7\text{F}_4$) increase with the temperature. This fact indicates the occurrence of Tb^{3+} -to- Eu^{3+} energy transfer, which seems to be much more pronounced in comparison with the solid-state spectra of pristine complexes **1** and **2** (Fig. S13–S16, ESI†), suggesting

the occurrence of a high impact of host silica nanoparticles on the luminescence properties. For instance, the relative intensities of the Tb^{3+} emissive transitions to the Eu^{3+} emissive ones in the solid state at room temperature are much lower in **MSN-1** than in pristine complex **1**: I_{550}/I_{615} goes from 3.8 to 0.6 and I_{550}/I_{700} goes from 22.0 to 0.8 once incorporated (Fig. 3b and Fig. S13b, ESI†). It means that the relative signals from the Eu^{3+} transitions have been multiplied by 6.3 at 615 nm and by 27.5 at 700 nm, compared to the one at 550 nm from Tb^{3+} . Thanks to the protective role of silica nanoparticles, the photoluminescent spectra have been recorded in water at room temperature for **MSN-1** and **MSN-2**. Note that this is not possible for the pristine complexes because they are not soluble in water. The excitation spectra recorded at room temperature in water (Fig. S11a and 12a, ESI†) show similar features to those in the solid state, demonstrating the main large excitation band at 312 nm and indicating the acetylacetonate sensitization and low-intensity characteristic transitions of both lanthanides, which are however less pronounced in comparison with the spectra in the solid state. The emission spectra also demonstrate similar features to the ones measured in the solid state but with a slightly different intensity ratio between different transitions (Fig. S11b and S12b, ESI†).

Theoretical calculations

Theoretical calculations have been performed first to explain the modification of the emission spectra of compounds **1** and **2** after encapsulation into the silica nanoparticles. Indeed, the Ln^{3+} ion can occupy nine positions in $[(\text{Tb}/\text{Eu})_9(\text{acac})_{16}(\mu_3\text{-OH})_8(\mu_4\text{-O})(\mu_4\text{-OH})]\cdot\text{H}_2\text{O}$, with the central site in a perfect C_4 point group symmetry, while the adjacent positions being close to a non-axial C_s group (Fig. 4b). When complexes **1** and **2** are incorporated into the mesostructured silica nanoparticles, the structure undergoes a slight change, which leads to a new coordination mode with the central oxygen atoms located on the C_4 axis (Fig. 4c). This changes the coordination number from 7 to 8 and the point group symmetry of the adjacent Ln^{3+} sites changes from C_s to C_{4v} (Fig. 4d). This explains the modification of the photoluminescence intensities of ${}^5\text{D}_0 \rightarrow {}^7\text{F}_2$ and ${}^5\text{D}_0 \rightarrow {}^7\text{F}_4$ emissions in **MSN-1** and **MSN-2**, which have only Ln^{3+} sites with the C_4 axis, resulting in a relatively high intensity of ${}^5\text{D}_0 \rightarrow {}^7\text{F}_4$ and a low intensity of ${}^5\text{D}_0 \rightarrow {}^7\text{F}_2$.^{57,58}

Second, the pairwise energy transfer rates between Tb^{3+} and Eu^{3+} ions were computed using the dipole–dipole ($W_{\text{d-d}}$, eqn (S3), ESI†), dipole–quadrupole ($W_{\text{d-q}}$, eqn (S4), ESI†), quadrupole–quadrupole ($W_{\text{q-q}}$, eqn (S5)†), exchange (W_{ex} , eqn (S6)†), and magnetic dipole–magnetic dipole ($W_{\text{md-md}}$, eqn (S7), ESI†) mechanisms.^{12,59–61} Tables S2 and S3 (ESI†) show the calculated energy transfer between Tb^{3+} and Eu^{3+} ions for the shortest distance ($R = 3.44$ Å) in **MSN-1** and **MSN-2** compounds at 300 K. To summarize the data more concisely, Fig. S17 (ESI†) shows all pairwise rates ($W_{\text{total}}^{\text{f}}$ and $W_{\text{total}}^{\text{b}}$) as a function of temperature for discrete donor–acceptor distances in **MSN-1** and **MSN-2** ($R = 3.44$, 3.52, and 3.55 Å) and in compounds **1** and **2** ($R = 3.62$, 3.65, and 3.73 Å). Visibly, the incorporation of



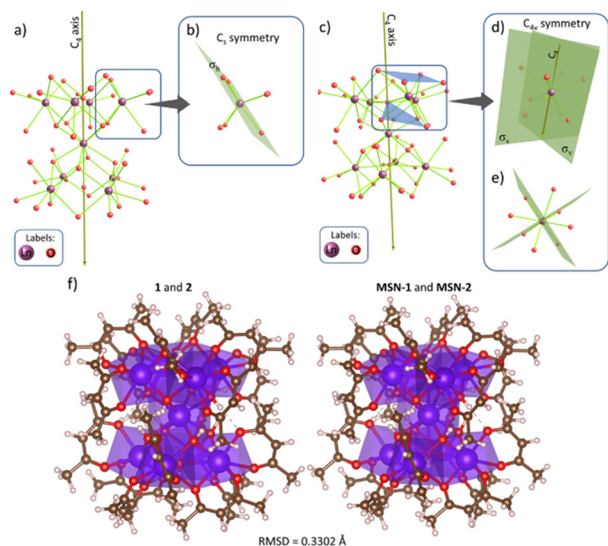


Fig. 4 (a) Backbone of **1** and **2** from the crystallographic structure displaying only the Ln and O atoms. The central Ln^{3+} ion is placed in a site with C_4 point group symmetry. (b) Adjacent Ln^{3+} ions are placed in a C_4 point group. The geometry was extracted from ref. 50. (c) Proposal of the structural distortion of the complexes inside MSN-1 and MSN-2. The central Ln^{3+} ion is still placed in a C_4 site; however, (d) adjacent Ln^{3+} ions are closer to the oxygen atoms (OH^- in the C_4 axis), changing their coordination number from 7 to 8 and, consequently, their point group symmetry from C_4 to C_{4v} , showing the C_4 element. (e) View of (d) along the C_4 axis. (f) Side-by-side structures for **1** and **2** in the solid-state (left panel) and their slightly distorted structure when incorporated in the MSN (right panel). The root-mean-square-deviation (RMSD) between these structures is 0.3302 Å (including H, O, C, and Ln atoms).

1 and **2** into the MSN structure leads to a shorter donor–acceptor distance and an increase in the pairwise rate by about 10 times. Also, it is worth mentioning that the exchange mechanism (W_{ex} , eqn (S6), ESI†) is the dominant one in the energy transfer process.

After calculating pairwise Tb^{3+} to Eu^{3+} energy transfer rates as a function of temperature (Fig. S17, ESI†), a homemade program was used to simulate a Monte-Carlo distribution of Tb^{3+} and Eu^{3+} ions in the host matrix. By expanding the unit cell from $1 \times 1 \times 1$ to $20 \times 20 \times 20$ (Fig. S18a, ESI†), containing 144 000 Tb^{3+} host sites, Eu^{3+} ions were randomly added until the desired amount was reached ($x = 5\%$ of Eu^{3+} for **1** and **MSN-1** and $x = 10\%$ of Eu^{3+} for **2** and **MSN-2**). The program then calculates the occurrence of Tb–Eu pairs as a function of donor–acceptor distance R and determines the average forward W^f and backward W^b energy transfer rates (eqn (S10) and (S11), ESI†).^{12,62} The results indicated that **MSN-1** and **MSN-2** have higher average energy transfer rates (W^f and W^b) compared to those of compounds **1** and **2** (Fig. S19, ESI†). This may be explained by the shorter Tb–Eu distance within the Ln_9 cluster when it is inserted inside the MSN. Also, **MSN-2** has a higher energy transfer rate than **MSN-1** due to its higher number of acceptors resulting from its stoichiometry. This result is supported by the more sudden decrease of $\text{Tb}^{3+} \text{ } ^5\text{D}_4 \rightarrow ^7\text{F}_5$ (donor) in **MSN-2** than in **MSN-1**, as depicted in Fig. S21 (ESI).†

X. Liu and coll. analysed the energy transfer confinement effect between Yb^{3+} ions in the orthorhombic KYb_2F_7 material.⁶³ They found that the energy transfer is more likely to occur inside the Yb^{3+} cluster (with Yb–Yb distances smaller than 3.55 Å) than between the clusters, where the shortest distance between Yb^{3+} ions is 3.80 Å. This probability was calculated to be over 10 times higher. When a similar analysis is conducted for **MSN-1** and **MSN-2**, the energy transfer rate inside the $(\text{Tb}/\text{Eu})_9$ compound is over 10^9 times higher than the rate between these molecules due to the larger minimal distance between Tb^{3+} ions in neighbour Tb_9 compounds (9.92 Å, Fig. S18a, ESI†). This can be seen in Fig. S20 (ESI),† which shows the ratio of the average energy transfer inside W_{in} and outside W_{out} the $(\text{Tb}/\text{Eu})_9$ compound.

It is worth noting that the $[(\text{Tb}/\text{Eu})_9(\text{acac})_{16}(\mu_3\text{-OH})_8(\mu_4\text{-O})(\mu_4\text{-OH})]\cdot\text{H}_2\text{O}$ structure may be considered as lanthanide molecular clusters $\{\text{Ln}_9\}$, which are highly regarded as the future of optical materials in different applications, such as luminescence thermometry, anti-counterfeiting, and molecular upconverters.⁵² The key advantage lies in the energy transfer process that occurs between the Ln^{3+} ions within the same cluster unit, enabling precise control over the performance at the individual cluster level. This feature offers significant benefits in terms of optimizing the desired functionalities and properties of these materials.

Luminescence thermometry

In order to investigate the possibility to use **MSN-1** and **MSN-2** as luminescent thermometers, the luminescence was investigated in water at different temperatures. Fig. 5 shows the luminescence spectra of **MSN-1** measured under 312 nm excitation in the 20–70 °C range (Fig. 5a), the corresponding LIR between Tb^{3+} and Eu^{3+} emissions by taking bands at 550 nm and 615 nm, respectively, (Fig. 5b) or bands at 545 nm and 700 nm, respectively (Fig. 5c). The wavelength ranges used to compute the integrated areas are 530–560 nm ($\text{Tb}^{3+}: ^5\text{D}_4 \rightarrow ^7\text{F}_5$) and 604–642 nm ($\text{Eu}^{3+}: ^5\text{D}_0 \rightarrow ^7\text{F}_2$) or 680–715 nm ($\text{Eu}^{3+}: ^5\text{D}_0 \rightarrow ^7\text{F}_4$). The error bars represent the standard deviation of average values obtained upon three consecutive temperature cycles. The temperature-dependent variation of the LIR parameters shows a second-degree polynomial correlation in the full temperature range of 20–70 °C and a linear correlation in the physiological domain (20–40 °C) indicative of a self-referencing temperature sensor.

The relative thermal sensitivity (S_r) is the parameter allowing the comparison of thermometric performance among different types of thermometers.⁶⁴ The S_r value represents the variation of the experimental parameter (LIR in the present case) per degree of temperature, expressed as:

$$S_r(T) = |\partial \text{LIR}(T) / \partial T| / \text{LIR}(T).$$

The temperature dependences of S_r with two different LIRs are shown in Fig. 5b and Fig. S22 (ESI).† The maximum of these curves estimated from the calibration data is equal to $1.4\% \text{ } ^\circ\text{C}^{-1}$ at 42.67 °C for $\text{LIR}(I_{550}/I_{700})$ and $1.1\% \text{ } ^\circ\text{C}^{-1}$ at 56.22 °C for $\text{LIR}(I_{550}/I_{615})$. **MSN-2** with a Tb/Eu ratio of 9/1 also



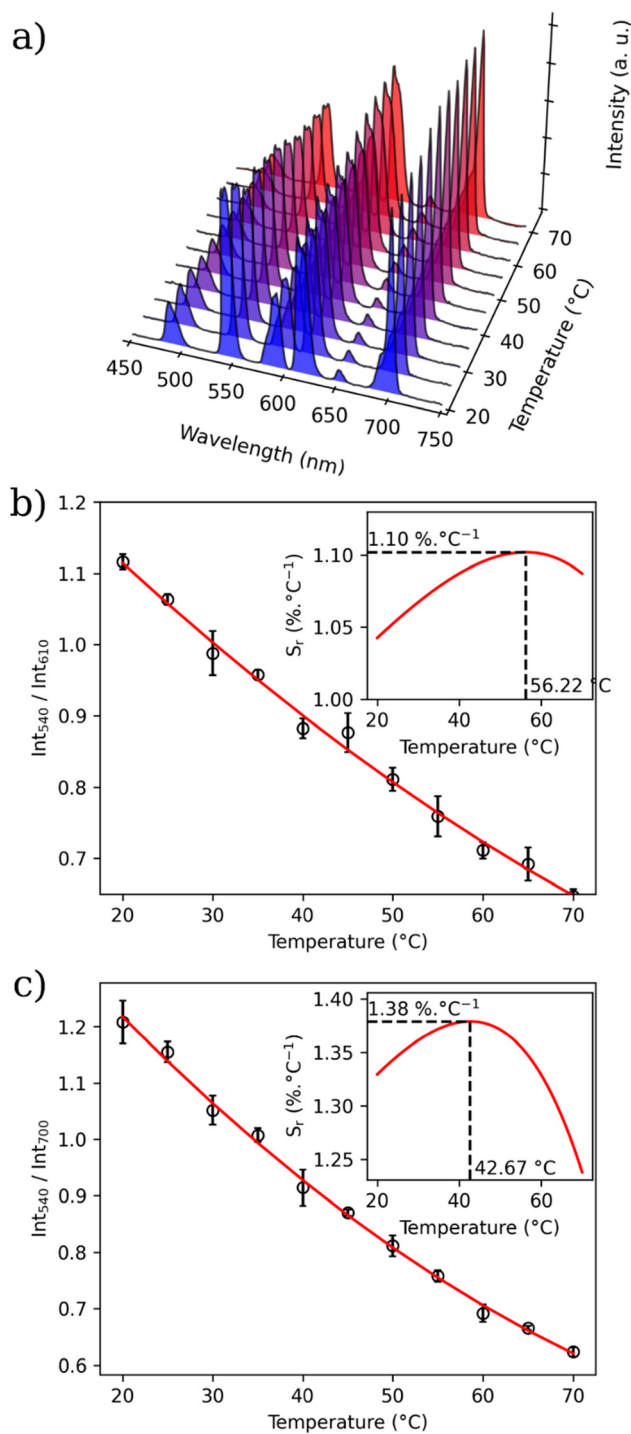


Fig. 5 (a) Emission spectra ($\lambda_{\text{ex}} = 312 \text{ nm}$) of **MSN-1** recorded at different temperatures ranging from 20 to 70 °C in water; (b) the corresponding LIR between the $^5\text{D}_4 \rightarrow ^7\text{F}_5$ (Tb^{3+}) and $^5\text{D}_0 \rightarrow ^7\text{F}_2$ (Eu^{3+}) transitions. The solid line represents a second-degree polynomial fitting. Integrated areas: 530–560 nm (Tb^{3+} : $^5\text{D}_4 \rightarrow ^7\text{F}_5$) and 604–642 nm (Eu^{3+} : $^5\text{D}_0 \rightarrow ^7\text{F}_2$). Inset: temperature dependence of S_r . Inset: temperature dependence of S_r . The error bars correspond to the standard error of the mean determined from three consecutive temperature cycles.

Table 2 Calibration parameters for thermometry measurements of **MSN-1** and **MSN-2**

	MSN-1	MSN-2
Temperature operating range	20–70 °C	20–70 °C
Maximal relative sensitivity (S_r) with LIR _{540/610} in water	1.1% °C ⁻¹ at 56.2 °C	2.2% °C ⁻¹ at 52.7 °C
Maximal relative sensitivity (S_r) with LIR _{540/700} in water	1.4% °C ⁻¹ at 42.7 °C	2.3% °C ⁻¹ at 56.2 °C
Uncertainty (δT) in water	0.05 °C	0.05 °C
Repeatability (RSD) in water	4.5%	5.6%
Maximal relative sensitivity (S_r) with LIR _{540/610} in PBS	4.10% °C ⁻¹ at 70.0 °C	
Photostability after continuous irradiation for 4 h in water	79% for $^5\text{D}_4 \rightarrow ^7\text{F}_5$ (550 nm)	82% for $^5\text{D}_0 \rightarrow ^7\text{F}_2$ (610 nm)

demonstrate the characteristics of a self-referencing temperature sensor with a slightly higher relative sensitivity of 2.26% °C⁻¹ at 56 °C (Table 2 and Fig. S22, ESI†). These maximal sensitivities are close to the frequently considered high relative thermal sensitivity ($\sim 1\% \text{ °C}^{-1}$).²⁰ Moreover, these values are coherent with the better S_r values obtained for different nanoparticles containing luminescent lanthanide thermometers working in water (see Table S1†).¹²

The repeatability of measurements, which corresponds to the variability among the measurements, is indicated by the relative standard deviation (RSD). Therefore, satisfactory repeatability was observed as the maximum RSD among the measurement values was lower than 4.5% for **MSN-1** and 5.6% for **MSN-2**.

The thermal uncertainty was also calculated as the smallest temperature change that can be measured, *i.e.*:

$$\partial T = |\partial \text{LIR}(T)/\text{LIR}(T)|/S_r(T).$$

The measured thermal uncertainty is very satisfactory for all samples: 0.05 °C for **MSN-1** and **MSN-2**. The calibration parameters are gathered in Table 2 along with several metric parameters that provide the thermometric performance in the operating temperature range.

We also estimated the protective role of the silica host taking into account that classical Ln^{3+} -based coordination compounds and, in particular, β -diketonates are well known for their instability even in the solid state.³⁰ The photostability of sample **MSN-1** was evaluated in water under continuous UV irradiation at 310 nm for 4 h using a 450 W xenon lamp as the excitation source. The inset of Fig. S24 (ESI)† displays the emission spectra recorded in water each 30 min and Fig. S24 (ESI)† shows the corresponding integrated intensity variation of $^5\text{D}_4 \rightarrow ^7\text{F}_5$ (550 nm) and $^5\text{D}_0 \rightarrow ^7\text{F}_2$ (610 nm) transitions with the irradiation time. The integrated intensities of the transitions decrease by only 21 and 18%, respectively, after 4 h of continuous irradiation, indicating a very good photostability of **MSN-1** in water upon irradiation.



Luminescence thermometry in PBS and in cells

To go one step further, we verify if our temperature nanosensor is operational in PBS and in living cells. For this, the **MSN-1** has been dispersed in PBS medium and the emission spectra have been recorded under 310 nm excitation in the temperature range of 20–70 °C (Fig. S25a, ESI†). The temperature dependence of the LIR taken between the emissions $^5D_4 \rightarrow ^7F_5$ at 550 nm (Tb^{3+}) and $^5D_0 \rightarrow ^7F_2$ at 615 nm (Eu^{3+}) is shown in Fig. S25b (ESI†) and the corresponding temperature dependence of S_r is presented in the inset of this figure. The result demonstrates that **MSN-1** is operational for temperature sensing in this range with a maximal thermal sensibility of $4.1\% \text{ } ^\circ\text{C}^{-1}$ at 70 °C (Table 2). Then, we check if temperature detection may also be performed in living cells. For this, **MSN-1** was incubated in various cell lines to study first its cytotoxicity. For this purpose, human MCF-7 cell lines were incubated with various concentrations from 0 to $200 \mu\text{g mL}^{-1}$ and cell viability was measured after 3 days of incubation. A relatively good cell viability of around 80% was observed for all concentrations, ranging from 5 to $200 \mu\text{g mL}^{-1}$, while for a very low concentration of $1 \mu\text{g mL}^{-1}$ the viability is equal to 90% (Fig. S26, ESI†). The TEM image shown in Fig. S27 (ESI†) indicates that the nanoparticles can be successfully internalized in living cells.

To perform proof-of-concept thermometry measurements under close conditions to what was done with **MSN-1** dispersed in water, human Y-29 cells were treated with $100 \mu\text{g mL}^{-1}$ **MSN-1** and incubated for 24 h. The Y-29 cell line was chosen as these cells are non-adherent ones. Luminescence measurements were performed in the Edinburgh spectrofluorimeter with the cells incubated with nanoparticles in PBS. The emission spectrum of this suspension at an excitation wavelength of 310 nm is shown in Fig. S28 (ESI†). Despite an important autofluorescence of the cells and PBS, the emission bands from Tb^{3+} and Eu^{3+} , coherent with the emission of **MSN-1** in water can be clearly observed. We can note a slight decrease in the relative intensity for the $^5D_0 \rightarrow ^7F_4$ transition of Eu^{3+} (at ca. 700 nm) compared to the emission spectrum in water. Emission spectra for the thermometric measurements were recorded in the 20–40 °C range adapted for living cells (Fig. 6a). The temperature dependences of the LIR (Fig. 6b) determined from those measurements indicate a good linear dependence ($R^2 = 0.98$). The calculated S_r value is high in this temperature range (over $3\% \text{ } ^\circ\text{C}^{-1}$) with a maximum of $8.6\% \text{ } ^\circ\text{C}^{-1}$ at 40 °C (inset of Fig. 6b). Therefore, these preliminary results show that **MSN-1** is operational in water, in PBS and in cells as luminescent nanosensors and when optimised will constitute good candidates for self-referencing thermometry measurements.

The difference in the calibration curves in water and cells indicates that an appropriate temperature calibration in each medium is necessary in order to provide accurate temperature sensing. Note that such comparative calibrations are very scarce in the literature and none yet for nanothermometers

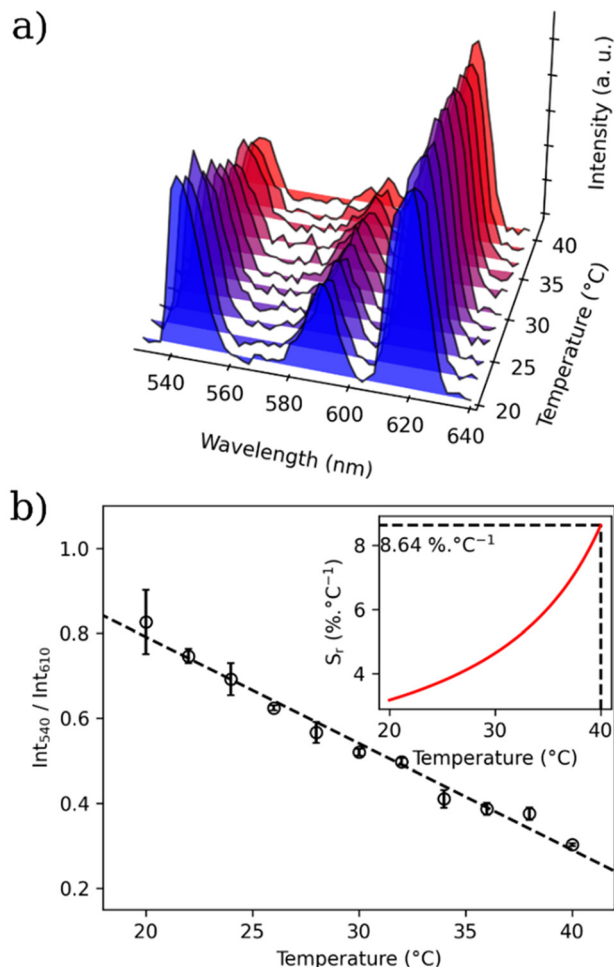


Fig. 6 (a) Emission spectra ($\lambda_{\text{ex}} = 310 \text{ nm}$) of Y-29 cells impregnated with **MSN-1** at different temperatures ranging from 20 to 40 °C measured in a suspension in PBS; (b) the corresponding LIR between the $^5D_4 \rightarrow ^7F_5$ (Tb^{3+}) and $^5D_0 \rightarrow ^7F_2$ (Eu^{3+}) transitions. The dotted line represents a linear fitting. Integrated areas: 530–560 nm (Tb^{3+} : $^5D_4 \rightarrow ^7F_5$) and 604–642 nm (Eu^{3+} : $^5D_0 \rightarrow ^7F_2$). Inset: temperature dependence of S_r . The error bars correspond to the standard error of the mean determined from three consecutive temperature cycles.

based on Ln^{3+} complexes using the intensity ratio method, as reported here. In particular, a recently published work by P. Rodríguez-Sevilla, D. Jacques and Q. A. Thompson clearly demonstrated differences in the calibration curves obtained under different environmental conditions or in the absence and presence of cell activity for two well-established nanothermometers, such as GFP and QDs and encouraged the community working in thermometry to approach the issue in a conscious manner.²⁷ In different environments the correlation can follow a different parametrization. Absorption, autofluorescence, and diffusion among other properties specific to each system are indeed expected to affect the luminescent probe in a different manner. Importantly, the calibration curve should remain consistent across different cycles in each environment.



Conclusion

In summary, stellate mesoporous silica nanoparticles dually functionalized with acetylacetonate moieties inside the pores and zwitterions on the nanoparticles' surface were used for the encapsulation of $[(\text{Tb}/\text{Eu})_9(\text{acac})_{16}(\mu_3\text{-OH})_8(\mu_4\text{-O})(\mu_4\text{-OH})]$ complexes to design self-calibrated nanothermometers working in water, in PBS and in living cells. The silica host plays a protective role in ensuring better colloidal and photothermal stability, providing the possibility to work in aqueous dispersions, which is not possible with the pristine compound. Two mixed lanthanide compounds with different $\text{Tb}^{3+}/\text{Eu}^{3+}$ ratios (19/1 and 9/1) were encapsulated into these silica nanoparticles for this purpose. The obtained functional nanoparticles present a size of *ca.* 90 nm and conserve their initial stellate-like morphology after the compounds' loading and pore clogging. The encapsulation of complexes around 0.5% (per unit of SiO_2 , *ie.* 4.5% unit of Ln^{3+} per unit of SiO_2) was proved by an ensemble of different characterisation techniques, including IR spectroscopy, STEM-EDS atomic mapping, nitrogen sorption, elemental and EDS analyses, as well as luminescence analysis. They present good colloidal stability for 48 h in water and in protein-rich media owing to the zwitterions grafted on the surface of the nanoparticles.

The investigations of the photoluminescence properties in the solid state permitted us to confirm the encapsulation of $[(\text{Tb}/\text{Eu})_9(\text{acac})_{16}(\mu_3\text{-OH})_8(\mu_4\text{-O})(\mu_4\text{-OH})]$ in the silica host. Indeed, the nanoparticles exhibit similar excitation and emission in comparison with the parent compounds with the evidence of the Tb^{3+} -to- Eu^{3+} energy transfer due to the relatively short distances between two lanthanide ions. On the other hand, some modifications in the solid-state emission spectra of nanoparticles compared to the ones of the free complexes indicate the occurrence of slight geometry modification of the latter, which can be induced by interactions with the acetylacetonate molecules of the silica. The theoretical simulations indicated that a modification of the coordination environment of the 7-coordinated Ln^{3+} site, which changes the coordination number from 7 to 8 and the point group symmetry from C_s to C_{4v} inducing a slight shortening of intramolecular Ln^{3+} - Ln^{3+} distances, clearly explains the observed high intensities of $^5\text{D}_0 \rightarrow ^7\text{F}_2$ and $^5\text{D}_0 \rightarrow ^7\text{F}_4$ emissions in **MSN-1** and **MSN-2** (which have only Ln^{3+} sites with the C_4 axis) and an increase in the pairwise energy transfer rate by about 10 times.

The photoluminescence spectra were recorded in water due to the protective role of the silica matrix. The spectra present similar features to the ones recorded in the solid state. The temperature dependence of the luminescence investigated in the 20–70 °C range in water indicates that these nanoparticles can be used as efficient nanothermometers with good photothermal stability, cyclability and repeatability (>95%). The best thermometer performance in water evidenced by the maximum relative sensitivity of 1.1% °C⁻¹ achieved at 42.67 °C for **MSN-1** and 2.3% °C⁻¹ at 56.17 °C for **MSN-2** is found among the best emissive temperature probes based on hybrid nanoparticles (see Table S1, ESI†). Moreover, the preliminary tests performed in living cells, even if the excitation wavenum-

ber is not adapted for safe biological measurements, indicate that the nanoprobe can also be operational for temperature sensing under these conditions. Our results also show that the proper temperature calibration in each medium is necessary in order to provide accurate temperature sensing. Therefore, these results demonstrate that the dually functionalized mesostructured stellate-like silica nanoparticles appeared as an excellent host for the encapsulation of luminescent coordination compounds to design emissive nanosensors and when optimised, will constitute excellent candidates for self-referencing thermometry for different applications in aqueous media including biology, catalysis, *etc.* The next step of our work is to provide stellate-like mesoporous silica-based nanothermometers containing lanthanide complexes emissive in the NIR domain and able to be excited in the visible region.

Author contributions

Conceptualization: S. S., G. F., J. L. and Y. G.; methodology: T. P., S. S., L. M. A. A., F. M., M. G.-B., G. F., B. A., L. B., J. L., L. C. and Y. G.; validation: T. P. and S. S.; formal analysis: T. P., S. S., Y. G., E. O., and A. N. C. N.; investigation: T. P., S. S., E. O., B. A., A. N. C. N., L. M. A. A., and M. G.-B.; resources: J. L. and Y. G.; data curation: T. P., S. S., G. F., and A. N. C. N.; writing – original draft preparation: T. P. and J. L.; writing – review and editing: S. S., G. F., B. A., L. B., J. L., L. C., L. M. A. A., M. G.-B. and Y. G.; visualization: J. L., L. C., L. B. and Y. G.; supervision: S. S., G. F., J. L., B. A. and Y. G.; project administration: J. L. and Y. G.; funding acquisition: J. L. and Y. G. All authors have read and agreed to the published version of the manuscript.

Conflicts of interest

There are no conflicts to declare.

Acknowledgements

T. P., J. L., G. F. and Y. G. thank the University of Montpellier and CNRS for financial support, B. A. and L. B. thank the French “Ministère de l'Enseignement Supérieur et de la Recherche (MESR)” as well as the Ecole Normale Supérieure de Lyon for the PhD funding (CDSN). The authors are grateful to the Platform of Analysis and Characterization (PAC) of ICGM for X-ray diffraction measurements and the MEA platform for the transmission electronic microscopy and STEM-BF/EDX measurements. The authors thank B. Baus-Lagarde (ICSM) for the ICP measurements. The work was also developed within the scope of the project CICECO-Aveiro Institute of Materials (UIDB/50011/2020 & UIDP/50011/2020) and The Shape of Water (PTDC/NAN-PRO/3881/2020) financed by Portuguese funds through the FCT/MEC and, when appropriate, co-financed by FEDER under the PT2020 Partnership Agreement. The support of the European Union's Horizon 2020 FET Open



program under grant agreement no. 801305 (NanoTBTEch) is also acknowledged.

References

- 1 M. D. Dramićanin, *J. Appl. Phys.*, 2020, **128**, 040902.
- 2 M. Quintanilla, M. Henriksen-Lacey, C. Renero-Lecuna and L. M. Liz-Marzán, *Chem. Soc. Rev.*, 2022, **51**, 4223–4242.
- 3 D. Jaque, B. D. Rosal, E. M. Rodríguez, L. M. Maestro, P. Haro-González and J. G. Solé, *Nanomedicine*, 2014, **9**, 1047–1062.
- 4 A. Nexha, J. J. Carvajal, M. C. Pujol, F. Díaz and M. Aguiló, *Nanoscale*, 2021, **13**, 7913–7987.
- 5 X. Qiu, Q. Zhou, X. Zhu, Z. Wu, W. Feng and F. Li, *Nat. Commun.*, 2020, **11**, 4.
- 6 O. A. Savchuk, P. Haro-González, J. J. Carvajal, D. Jaque, J. Massons, M. Aguiló and F. Díaz, *Nanoscale*, 2014, **6**, 9727–9733.
- 7 M. Bettinelli, L. Carlos and X. Liu, *Phys. Today*, 2015, **68**, 38–44.
- 8 S. Goderski, M. Runowski, P. Woźny, V. Lavín and S. Lis, *ACS Appl. Mater. Interfaces*, 2020, **12**, 40475–40485.
- 9 Y. Cui, H. Xu, Y. Yue, Z. Guo, J. Yu, Z. Chen, J. Gao, Y. Yang, G. Qian and B. Chen, *J. Am. Chem. Soc.*, 2012, **134**, 3979–3982.
- 10 L. Zhang, Y. Xie, T. Xia, Y. Cui, Y. Yang and G. Qian, *J. Rare Earths*, 2018, **36**, 561–566.
- 11 D. Zhao, X. Rao, J. Yu, Y. Cui, Y. Yang and G. Qian, *Inorg. Chem.*, 2015, **54**, 11193–11199.
- 12 V. Trannoy, A. N. Carneiro Neto, C. D. S. Brites, L. D. Carlos and H. Serier-Brault, *Adv. Opt. Mater.*, 2021, **9**, 2001938.
- 13 J. Rocha, C. D. S. Brites and L. D. Carlos, *Chem. – Eur. J.*, 2016, **22**, 14782–14795.
- 14 A. Cadiau, C. D. S. Brites, P. M. F. J. Costa, R. A. S. Ferreira, J. Rocha and L. D. Carlos, *ACS Nano*, 2013, **7**, 7213–7218.
- 15 L. Li, Y. Zhu, X. Zhou, C. D. S. Brites, D. Ananias, Z. Lin, F. A. A. Paz, J. Rocha, W. Huang and L. D. Carlos, *Adv. Funct. Mater.*, 2016, **26**, 8677–8684.
- 16 D. M. Lyubov, A. N. C. Neto, A. Fayoumi, K. A. Lyssenko, V. M. Korshunov, I. V. Taydakov, F. Salles, Y. Guari, J. Larionova, L. D. Carlos, J. Long and A. A. Trifonov, *J. Mater. Chem. C*, 2022, **10**, 7176–7188.
- 17 M. Suzuki, V. Tseeb, K. Oyama and S. Ishiwata, *Biophys. J.*, 2007, **92**, L46–L48.
- 18 A. A. Ansari, A. K. Parchur, M. K. Nazeeruddin and M. M. Tavakoli, *Coord. Chem. Rev.*, 2021, **444**, 214040.
- 19 C. D. S. Brites, A. Millán and L. D. Carlos, in *Handbook on the Physics and Chemistry of Rare Earths*, ed. J.-C. Bunzli and V. K. Pecharsky, Elsevier, 2016, vol. 49, pp. 339–427.
- 20 C. D. S. Brites, S. Balabhadra and L. D. Carlos, *Adv. Opt. Mater.*, 2019, **7**, 1801239.
- 21 C. D. S. Brites, P. P. Lima, N. J. O. Silva, A. Millán, V. S. Amaral, F. Palacio and L. D. Carlos, *Nanoscale*, 2012, **4**, 4799–4829.
- 22 D. Jaque and F. Vetrone, *Nanoscale*, 2012, **4**, 4301–4326.
- 23 Luminescence Thermometry: Methods, Materials and Applications - 1st Edition, <https://www.elsevier.com/books/luminescence-thermometry/dramicanin/978-0-08-102029-6>, (accessed June 13, 2022).
- 24 Z. Shi, Y. Duan, X. Zhu, Q. Wang, D. Li, K. Hu, W. Feng, F. Li and C. Xu, *Nanotechnology*, 2018, **29**, 094001.
- 25 X. Di, D. Wang, J. Zhou, L. Zhang, M. H. Stenzel, Q. P. Su and D. Jin, *Nano Lett.*, 2021, **21**, 1651–1658.
- 26 R. Piñol, J. Zeler, C. D. S. Brites, Y. Gu, P. Téllez, A. N. Carneiro Neto, T. E. da Silva, R. Moreno-Loshuertos, P. Fernandez-Silva, A. I. Gallego, L. Martinez-Lostao, A. Martínez, L. D. Carlos and A. Millán, *Nano Lett.*, 2020, **20**, 6466–6472.
- 27 P. Rodríguez-Sevilla, G. Spicer, A. Sagrera, A. P. Adam, A. Efeyan, D. Jaque and S. A. Thompson, *Adv. Opt. Mater.*, 2020, 2201664.
- 28 J.-C. Bünzli and S. Eliseeva, in *Lanthanide Luminescence*, 2010, vol. 7, pp. 1–45.
- 29 J.-C. G. Bünzli and C. Piguet, *Chem. Soc. Rev.*, 2005, **34**, 1048–1077.
- 30 P. P. Lima, M. M. Nolasco, F. A. A. Paz, R. A. S. Ferreira, R. L. Longo, O. L. Malta and L. D. Carlos, *Chem. Mater.*, 2013, **25**, 586–598.
- 31 M. Hasegawa, H. Ohmagari, H. Tanaka and K. Machida, *J. Photochem. Photobiol., C*, 2022, **50**, 100484.
- 32 C. D. S. Brites, P. P. Lima, N. J. O. Silva, A. Millán, V. S. Amaral, F. Palacio and L. D. Carlos, *Adv. Mater.*, 2010, **22**, 4499–4504.
- 33 Y. Takei, S. Arai, A. Murata, M. Takabayashi, K. Oyama, S. Ishiwata, S. Takeoka and M. Suzuki, A Nanoparticle-Based Ratiometric and Self-Calibrated Fluorescent Thermometer for Single Living Cells, <https://pubs.acs.org/doi/pdf/10.1021/nn405456e>, (accessed June 13, 2022).
- 34 Ferdinandus, S. Arai, S. Takeoka, S. Ishiwata, M. Suzuki and H. Sato, *ACS Sens.*, 2016, **1**, 1222–1227.
- 35 A. M. Kaczmarek, Y. Maegawa, A. Abalymov, A. G. Skirtach, S. Inagaki and P. Van Der Voort, *ACS Appl. Mater. Interfaces*, 2020, **12**, 13540–13550.
- 36 A. M. Kaczmarek, R. V. Deun and P. V. D. Voort, *J. Mater. Chem. C*, 2019, **7**, 4222–4229.
- 37 D. Mara, A. M. Kaczmarek, F. Artizzu, A. Abalymov, A. G. Skirtach, K. Van Heck and R. Van Deun, *Chem. – Eur. J.*, 2021, **27**, 6479–6488.
- 38 K. Nigoghossian, Y. Messaddeq, D. Boudreau and S. J. L. Ribeiro, *ACS Omega*, 2017, **2**, 2065–2071.
- 39 R. Piñol, C. D. S. Brites, R. Bustamante, A. Martínez, N. J. O. Silva, J. L. Murillo, R. Cases, J. Carrey, C. Estepa, C. Sosa, F. Palacio, L. D. Carlos and A. Millán, *ACS Nano*, 2015, **9**, 3134–3142.
- 40 V. Kalaparathi, B. Peng, S. A. M. A. Peerzade, S. Palantavida, B. Maloy, M. E. Dokukin and I. Sokolov, *Nanoscale Adv.*, 2021, **3**, 5090–5101.
- 41 B. Francis, B. Neuhaus, M. L. P. Reddy, M. Eppel and C. Janiak, *Eur. J. Inorg. Chem.*, 2017, **2017**, 3205–3213.
- 42 Y. A. Grechkin, S. L. Grechkina, E. A. Zaripov, S. V. Fedorenko, A. R. Mustafina and M. V. Berezovski, *Biomedicine*, 2020, **8**, 14.



- 43 H. Ma, B. Song, Y. Wang, D. Cong, Y. Jiang and J. Yuan, *Chem. Sci.*, 2017, **8**, 150–159.
- 44 C. Gaillard, P. Adumeau, J.-L. Canet, A. Gautier, D. Boyer, C. Beaudoin, C. Hesling, L. Morel and R. Mahiou, *J. Mater. Chem. B*, 2013, **1**, 4306–4312.
- 45 A. P. Duarte, M. Gressier, M.-J. Menu, J. Dexpert-Ghys, J. M. A. Caiut and S. J. L. Ribeiro, *J. Phys. Chem. C*, 2012, **116**, 505–515.
- 46 C. Malba, U. P. Sudhakaran, S. Borsacchi, M. Geppi, F. Enrichi, M. M. Natile, L. Armelao, T. Finotto, R. Marin, P. Riello and A. Benedetti, *Dalton Trans.*, 2014, **43**, 16183–16196.
- 47 X. Du and S. Z. Qiao, *Small*, 2015, **11**, 392–413.
- 48 V. Polshettiwar, D. Cha, X. Zhang and J. M. Basset, *Angew. Chem., Int. Ed.*, 2010, **49**, 9652–9656.
- 49 T. Pelluau, S. Sene, B. Garcia-Cirera, B. Albela, L. Bonneviot, J. Larionova and Y. Guari, *Nanomaterials*, 2022, **12**, 1136.
- 50 S. Petit, F. Baril-Robert, G. Pilet, C. Reber and D. Luneau, *Dalton Trans.*, 2009, 6809–6815.
- 51 D. Guettas, C. M. Balogh, C. Sonnevile, Y. Malicet, F. Lepoivre, E. Onal, A. Fateeva, C. Reber, D. Luneau, O. Maury and G. Pilet, *Eur. J. Inorg. Chem.*, 2016, **2016**, 3932–3938.
- 52 D. A. Gállico, C. M. S. Calado and M. Murugesu, *Chem. Sci.*, 2023, **14**, 5827–5841.
- 53 B. Yuan, X. He, Y. Chen and K. Wang, *Macromol. Chem. Phys.*, 2011, **212**, 2378–2388.
- 54 S. Chen, S. Chen, S. Jiang, Y. Mo, J. Tang and Z. Ge, *Surf. Sci.*, 2011, **605**, L25–L28.
- 55 Z. G. Estephan, J. A. Jaber and J. B. Schlenoff, *Langmuir*, 2010, **26**, 16884–16889.
- 56 K. Binnemans, *Coord. Chem. Rev.*, 2015, **295**, 1–45.
- 57 M. Bettinelli, A. Speghini, F. Piccinelli, A. N. C. Neto and O. L. Malta, *J. Lumin.*, 2011, **131**, 1026–1028.
- 58 N. S. Kariaka, V. A. Trush, V. V. Dyakonenko, S. V. Shishkina, S. S. Smola, N. V. Rusakova, T. Y. Sliva, P. Gawryszewska, A. N. Carneiro Neto, O. L. Malta and V. M. Amirkhanov, *ChemPhysChem*, 2022, **23**, e202200129.
- 59 A. N. Carneiro Neto, R. T. Moura, A. Shyichuk, V. Paterlini, F. Piccinelli, M. Bettinelli and O. L. Malta, *J. Phys. Chem. C*, 2020, **124**, 10105–10116.
- 60 O. L. Malta, *J. Non-Cryst. Solids*, 2008, **354**, 4770–4776.
- 61 A. N. Carneiro Neto, R. T. Moura and O. L. Malta, *J. Lumin.*, 2019, **210**, 342–347.
- 62 X. Qin, A. N. Carneiro Neto, R. L. Longo, Y. Wu, O. L. Malta and X. Liu, *J. Phys. Chem. Lett.*, 2021, **12**, 1520–1541.
- 63 J. Wang, R. Deng, M. A. MacDonald, B. Chen, J. Yuan, F. Wang, D. Chi, T. S. Andy Hor, P. Zhang, G. Liu, Y. Han and X. Liu, *Nat. Mater.*, 2014, **13**, 157–162.
- 64 A. Bednarkiewicz, L. Marciniak, L. D. Carlos and D. Jaque, *Nanoscale*, 2020, **12**, 14405–14421.

